COMMUNICATION

Check for updates

Engineering of robust conjugated polymer-based aerogels *via* surface-initiated polycondensation towards sunlight-driven seawater desalination and uranium extraction†

Yuan Chen,‡[ab] Guang-en Fu,‡[a] Yu-xiang Zhao,[a] Ke Wang,[a] Meng-wei Chen,[a] Qiang Ma, [iD][a] Shan Li,[a] Jun-Yi Han,[a] Li-sha Liang,[a] Wen-kai Zhao,[a] Peng Xiao, [iD][a] Sheng Wang,*[b] Tao Chen [iD] *[a] and Tao Zhang [iD] *[a]

The aerogels with low thermal conductivity and cross-linked 3D networks can be easily integrated with functional materials to maximize their functionalities, realizing diverse applications such as photothermal seawater desalination and photocatalytic uranium extraction. Sp^{2}C-conjugated porous polymers (sp^{2}C-CPPs) with robust and conjugated C=C linkages are ideal photosensitizers for these applications, owing to their exceptional semiconducting properties as well as chemical stability. However, the limited processability and collectability of as-synthesized sp^{2}C-CPP powders impede their extended applications. Herein, we report the preparation of robust sp^{2}C-CPP (DHA-TMT and DBD-TMT) based aerogels *via* surface-initiated aldol polycondensation (SI-AP). The fully conjugated C=C skeletons and electron-donating groups (–OH) endow the sp^{2}C-CPP aerogels with excellent photothermal conversion efficiency (95.6%) and strong affinity for uranium adsorption. In particular, the DHA-TMT aerogel with hydrophilic porous channel exhibits a superb evaporation performance achieving ∼1.55 kg m^{-2} h^{-1} under AM 1.5 G while the fast mass transfer caused by photothermal conversion increases the uranium extraction capacity up to 1200 mg m^{-2} in simulated seawater. Moreover, the sp^{2}C-CPP aerogels demonstrate high stability under strong acid, base and brine solutions. This work shows a strategy for the preparation of uniform and high stability sp^{2}C-CPP-based aerogels to simultaneously enhance their photothermal and photocatalytic performance.

New concepts

This work shows a strategy for the preparation of uniform and high stability sp^{2}C-CPP-based aerogels to simultaneously enhance their photothermal and photocatalytic performance. Herein, we demonstrate the preparation of robust sp^{2}C-CPP based aerogels *via* surface-initiated aldol polycondensation (SI-AP). Benefiting from the extended π-conjugated structure and the high-density –OH groups, the resultant sp^{2}C-CPP-based aerogels exhibit a broad light-harvesting range extended to 2500 nm and excellent photothermal conversion efficiency. In particular, the DHA-TMT aerogel with hydrophilic porous channel exhibits a superb evaporation performance achieving ∼1.55 kg m^{-2} h^{-1} under AM 1.5 G. Meanwhile, the DHA-TMT-based aerogels exhibit exceptional photothermal conversion efficiency, which significantly enhances ion transfer. The uranium extraction ability through the fast mass transfer caused by photothermal conversion improves the original adsorption capacity from 280 (under dark) to 1200 mg m^{-2}.

Introduction

Conjugated polymer aerogels (CPAs) are a class of multifunctional materials constructed through conjugated bonds,[1–3] integrating the excellent optoelectronic properties of conjugated polymers[4,5] with the high porosity and thermal insulating properties of aerogels.[6–9] Therefore, CPAs are widely applied in a range of fields like desalination,[10,11] photocatalysis,[12,13] air water harvesting[14,15] and adsorption.[16,17] However, traditional sol–gel and template-assisted methods for preparing freestanding CPAs encounter a barrier in terms of extensibility, such as the requirement for demanding conditions, such as supercritical CO_2 drying,[18] high temperature,[19,20] and specific synthesis systems,[21] and the as-prepared CPAs exhibit limited mechanical strength and uniformity.[22,23] An effective strategy to address these challenges is preparing CPAs by surface-initiated aldol polycondensation (SI-AP) and in situ growth on pre-existing robust SiO_2 aerogel substrates.[24,25] Compared with other physical methods,[26–29] the SI-AP strategy enables strong surface covalent bonding between the conjugated polymer and SiO_2 aerogel, achieving structural designability and excellent

[a] Key Laboratory of Advanced Marine Materials, Ningbo Institute of Materials Technology and Engineering, Chinese Academy of Sciences, Ningbo 315201, China. E-mail: tao.chen@nimte.ac.cn, tzhang@nimte.ac.cn

[b] School of Materials Science and Engineering, Zhejiang Sci-Tech University, Hangzhou 310018, China. E-mail: wangsheng@zstu.edu.cn

† Electronic supplementary information (ESI) available. See DOI: https://doi.org/10.1039/d4mh01055h

‡ This work is dedicated to the 20th anniversary of the Ningbo Institute of Materials Technology and Engineering (NIMTE). Y. Chen and G. Fu contributed equally to this work.

mechanical properties for stable operation in harsh marine environments.[30,31]

Aldol polycondensation, as an efficient method to construct C=C linkages through the reaction between aldehydes and acidic terminal methyl groups, has been extensively utilized to synthesize sp²C-conjugated porous polymers (sp²C-CPPs).[32–34] The resultant sp²C-CPP powders generally share high chemical stability and exceptional optoelectronic properties,[35–40] including light-harvesting capability[41,42] and high charge carrier mobility[43–45] due to their extended π-conjugation and robust skeletons, which render them highly desirable in numerous solar-driven energy conversion fields, such as photothermal seawater desalination and photocatalytic uranium extraction.[4,46] Nevertheless, the typical powder morphology and insolubility of sp²C-CPPs impede their practical application and recyclability.[47] As such, applying SI-AP to fabricate sp²C-CPP-based aerogels would be promising to surpass the inherent properties of powders and shape them into diverse forms towards desired applications.

Herein, we show the synthesis of two sp²C-CPP-based aerogels (DHA-TMT & DBD-TMT) through SI-AP on commercially available SiO₂ aerogels. Benefiting from the extended π-conjugated structure and the high-density –OH groups, the resultant sp²C-CPP-based aerogels exhibit a broad light-harvesting range extended to 2500 nm and excellent photothermal conversion efficiency (∼71.8 °C under AM 1.5G). Furthermore, the hydrophilic porous channel and robust skeleton endow the aerogels with remarkable seawater desalination performance (1.55 kg m⁻² h⁻¹) and high stability. Meanwhile, the DHA-TMT-based aerogels demonstrate exceptional photothermal conversion efficiency, significantly enhancing ion transfer and promoting uranium extraction capacity up to 1200 mg m⁻². This work presents the design and synthesis of robust and high-performance sp²C-CPP-based aerogels for simultaneous sunlight-driven seawater desalination and uranium extraction.

Results and discussion

Preparation and characterization of the sp²C-CPPs

Firstly, to explore the effect of varying conjugation degree on the photothermal properties of the materials, two sp²C-CPPs with different structures were synthesized (Fig. 1B). The sp²C-CPPs are synthesized via an in situ on surface-initiated strategy on the aerogel.

As shown in Fig. 1A, a self-assembled monolayer (SAM) of 3-aminopropyltrimethoxysilane (APTES) is created on an aerogel with a native oxidized layer. The comprehensive XPS spectra and high-resolution C 1s spectra of aerogel-APTES reveal distinct new N 1s and C–N peaks, respectively, providing compelling evidence for the successful grafting of APTES onto the aerogels (Fig. S1, ESI†). Next, the SAM-modified aerogel is immersed in a solution containing 2,4,6-trimethyl-1,3,5-triazine (TMT) and either 2,5-dihydroxy-1,4-benzenedicarboxaldehyde (DHA)/4′,4′-biphenyldicarboxaldehyde or 3′,3-dihydroxy (DBD) at 150 °C for three days to produce uniform DHA-TMT and DBD-TMT aerogels through

in situ growth (Fig. S2, ESI†). During the in situ growth process of DHA-TMT and DBD-TMT aerogels, Brønsted acid acts as a catalyst for both Schiff base formation and aldol condensation reactions resulting in grafting of an olefin-linked sp²C-CPP layer on the aerogel. The successful preparation of sp²C-CPPs was proven by Fourier transform infrared (FTIR) spectroscopy (Fig. 1C and D). In the FTIR spectra of both groups in DHA-TMT and DBD-TMT, a sharp decrease of the stretching vibration peak of C=O (1668 cm⁻¹, 1662 cm⁻¹) was observed; meanwhile, new peaks attributed to the C=C stretch band appeared at 1632 cm⁻¹ and 1617 cm⁻¹, confirming that the sp²C-CPPs of vinylene linkages were successfully formed. Scanning electron microscopy (SEM) measurements show that both sp²C-CPPs have globular morphology (Fig. 1E and F) and it should be noted that the blank sample fiber has a smooth surface with no isolated globular particles (Fig. S3, ESI†), evidencing that the 2D sp²C-CPPs grow in situ along the surface of the aerogel. In addition, SEM images show a rougher surface with more spherical particles in the DHA-TMT aerogel, which enhance light absorption through multiple internal reflections and scattering (Fig. 1E and F inset). Meanwhile, the rough surface also improved solar utilization efficiency and promoted a larger contact area with uranyl ions (Fig. S4, ESI†). Additionally, the water contact angle test results demonstrate that the blank aerogel was hydrophobic while the sp²C-CPP aerogel exhibits exceptional hydrophilicity due to the abundant presence of hydroxyl groups within its structure (Fig. S5, ESI†). The mechanical stiffness was assessed through a uniaxial quasi-static compression test. The mechanical properties of the blank aerogel and DHA aerogel are similar, revealing that sp²C-CPP coating has a relatively small impact on mechanical strength (Fig. S6 and S7, ESI†). Fig. S8a (ESI†) illustrates the strain–stress relationship of the sp²C-CPP aerogel at various compression strains (30%, 50%, and 70%). It is evident that the aerogel material predominantly exhibits a densification regime, with its stress exponentially increasing beyond a strain of 50%. The compressive strength rises with the increase in compressive strain, reaching a maximum value at 70% (approximately 0.63 MPa). The sp²C-CPP aerogel underwent compression fatigue tests, and after 10 load-to-unload cycles at a strain of 70%, it demonstrated the ability to retain approximately 70% of its initial maximum stress, exhibiting its exceptional mechanical strength (Fig. S8b and c, ESI†). Furthermore, the microscopic measurement demonstrated that sp²C-CPP aerogel still retains fibrous structure after compression fatigue testing. Moreover, the sp²C-CPP aerogels demonstrate exceptional chemical and thermal stabilities as evidenced by thermogravimetric analysis (TGA) and acid/base (12 M HCl or 12 M NaOH) immersion tests (Fig. S9, ESI†).

Efficient solar-powered water evaporation of sp²C-CPP aerogels

As shown in Fig. 2A, in the evaporation system, polystyrene foam was used to provide buoyancy, and cotton thread was employed to pump water from the bulk water for continuous and stable evaporation (Fig. S10, ESI†). To further investigate the light absorption performance, the light absorption properties of both sp²C-CPP aerogels were characterized by UV-vis-NIR spectroscopy (Fig. 2B). DHA-TMT aerogel showed relatively low
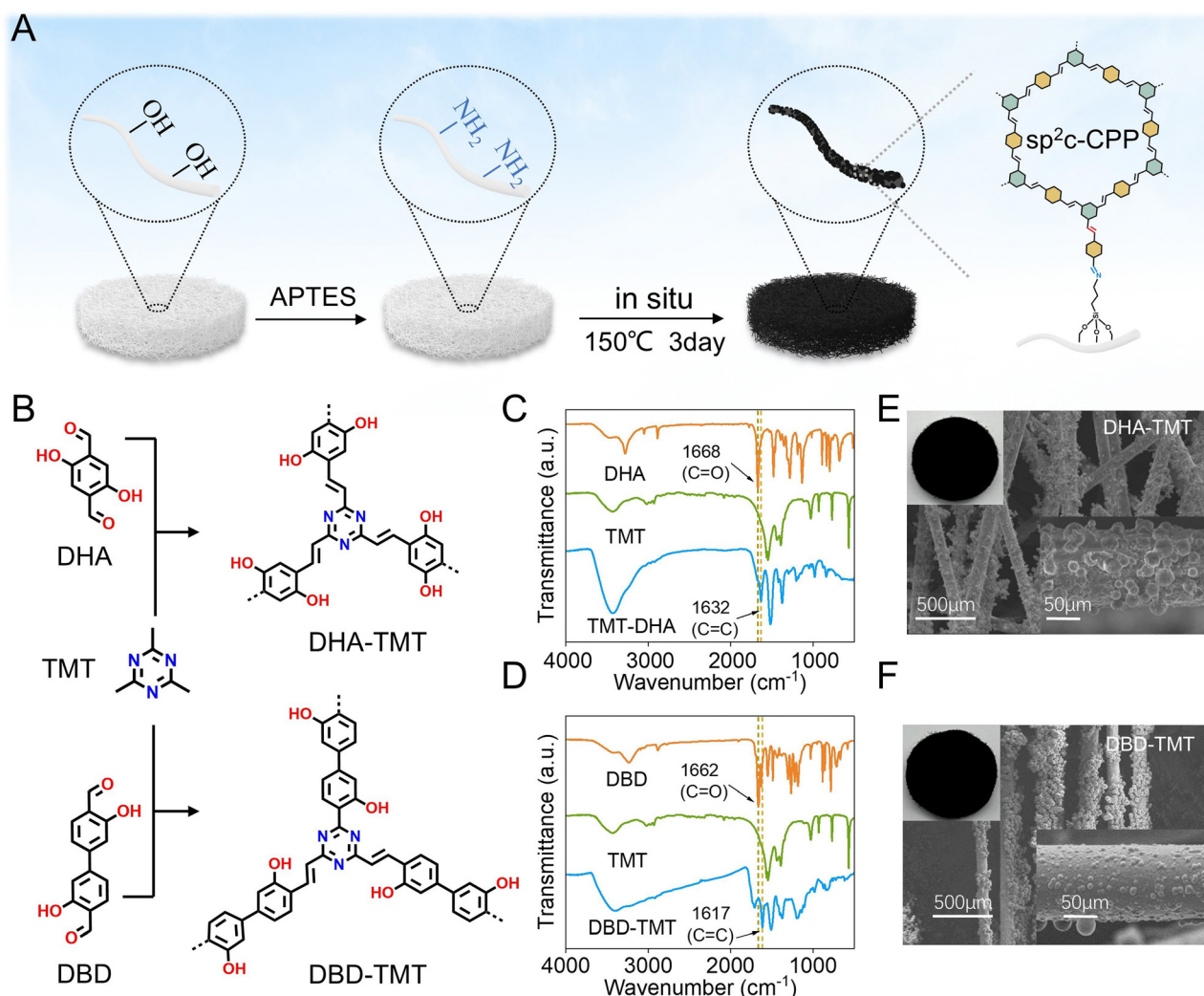
Fig. 1 (A) Schematic of the synthesis of sp²C-CPPs on aerogels through surface-initiated aldol polycondensation. (B) The theoretical structure of DHA-TMT and DBD-TMT. (C) and (D) FT-IR spectra of DHA, DBD, TMT, DHA-TMT CPP, and DBD-TMT CPP. (E) and (F) Photograph and SEM images of DHA-TMT aerogels and DBD-TMT aerogels.

light transmittance and reflectance over the entire solar spectrum compared with DBD-TMT aerogel, indicating that the DHA-TMT aerogel possessed more excellent light absorption performance. In addition to the rougher inner surface, the higher degree of conjugation of the DHA-TMT aerogel was another reason for the more excellent light absorption performance. Sp²C-CPPs are a new class of organic semiconductor materials follow the electron–hole generation and relaxation photothermal conversion mechanism. Organic polymers with highly planar backbones have the ability to enhance π-conjugation and facilitate electron–hole pair separation. Consequently, the extended π-conjugated plane structure, formed by hydroquinone units as building blocks with an elevated degree of conjugation, exhibits improved photothermal conversion efficiency. Furthermore, we used an IR camera to observe and record the temperature rise curve and photos of both sp²C-CPP aerogel evaporation devices under 1 sun (Fig. 2C and Fig. S11, ESI†). Compared with the dry DBD-TMT aerogel with a value of 65.5 °C

within 300 s, the DHA-TMT aerogel sample can reach up to 71.8 °C within 300 s under 1 sun irradiation. The results show that the higher the conjugation degree of sp²C-CPPs, the stronger the photothermal conversion ability.

We found that even though the absorption of water molecules has a high specific capacity, the surface temperature of the sp²C-CPP aerogels can reach almost 40 °C (Fig. S12 and S13, ESI†). Because of the low thermal conductivity of the aerogel, it has a good thermal insulation effect and greatly reduces the possible thermal diffusion, maximizing the use of converted solar energy. Then we tested the evaporation rate of both evaporators by optical concentrators. As shown in Fig. 2D, the water evaporation rates of the DHA-TMT and DBD-TMT aerogels were calculated to be 1.55 kg m⁻² h⁻¹ and 1.15 kg m⁻² h⁻¹ under 1 kW m⁻². It is worth noting that, with the gradual increase in solar irradiance, the water evaporation rate of sp²C-CPPs shows an almost linear growth trend. This implies that the performance of sp²C-CPPs remains relatively consistent
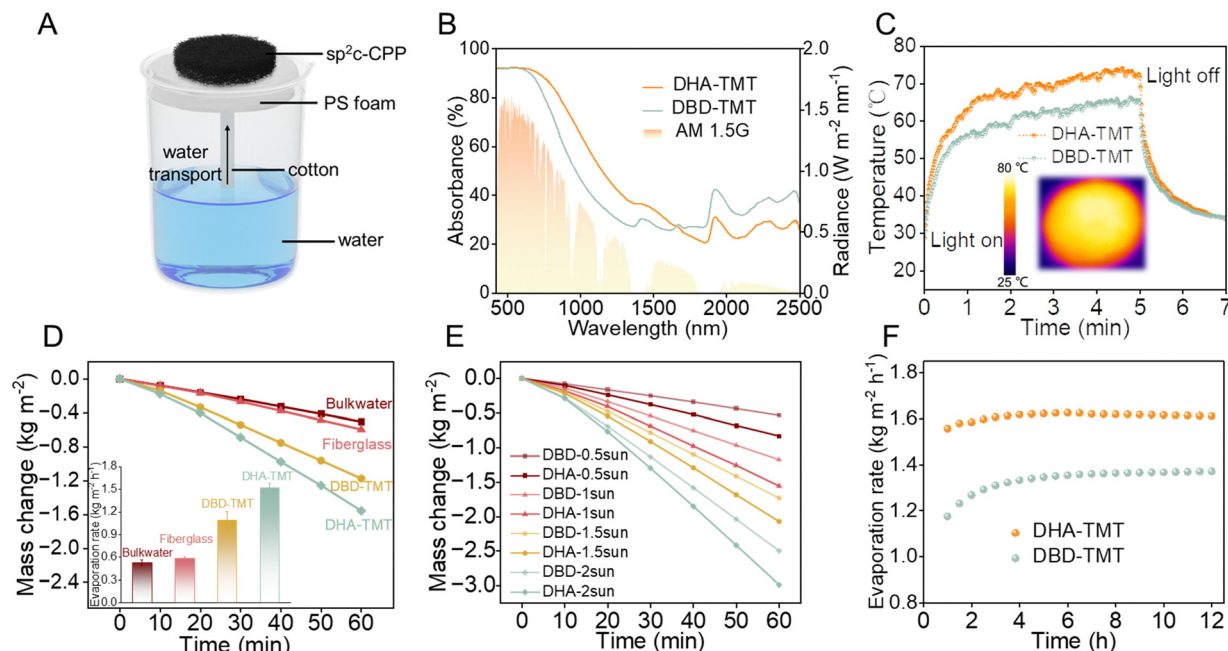
Fig. 2 (A) Scheme of the setup used in the water evaporation test. (B) The UV absorption spectra of different samples in the wavelength range of 400 to 2500 nm and comparison with the standard AM 1.5 G spectrum filter. (C) Temperature *versus* time curves of DHA-TMT aerogels and DBD-TMT aerogels. (D) Mass change *versus* time curves of bulk water, fiberglass, DHA-TMT aerogels, and DBD-TMT aerogels under 1 sun irradiation. Water evaporation rate from bulk water, fiberglass, and DHA-TMT, DBD-TMT under 1 sun irradiation (inset). (E) Mass change *versus* time curves of DHA-TMT and DBD-TMT evaporators under different optical concentrations. (F) DHA-TMT and DBD-TMT evaporator evaporation rate in simulated seawater for 12 hours.

under different solar radiation conditions, demonstrating predictable stability (Fig. 2E). Surprisingly, the water evaporation rates of the DHA-TMT aerogel reached 0.7 kg m^{-2} h^{-1} of 0.5 sun irradiation for 1 h. This shows that even in places where sunlight is insufficient, the evaporation device can achieve a good evaporation effect (Fig. S14a, ESI†).

Meanwhile, we found that both aerogel samples still maintained a high evaporation rate after 10 cycles and 12 hours in 3.5 wt% seawater (Fig. 2F and Fig. S14b, ESI†). Moreover, the evaporation rate and efficiency were not significantly reduced by experiments at high-concentrations as high as 25 wt% (Fig. S14c, ESI†), which indicates the effectiveness of seawater, and no solid salt was deposited on the surface of the aerogel after 1 hour of evaporation, showing the concentration self-driven salt-resistance of the sp^{2}C-CPP aerogels.

Self-driven salt resistance mechanism of the sp^{2}C-CPP aerogels

High salt-resistance is a key property of evaporators to achieve desalination at a high evaporation rate. In general, one of the mechanisms for salt mitigation is salt ion diffusion backflow, which requires a stable and efficient water supply capacity of the evaporator, as well as macro-channels. So we have employed a simple method to investigate the self-driven salt resistance mechanism of sp^{2}C-CPP aerogels. 0.5 gram of solid NaCl was placed on the surface of sp^{2}C-CPP aerogel and floated in 200 mL DI water. Upon contact with water, the sp^{2}C-CPPs aerogel was soaked rapidly due to the capillary effect, and then we observed that the solid salt dissolved in a short time and formed a concentrated salt solution on the surface of the sp^{2}C-CPPs aerogel (Fig. 3A). And as new liquid flowed into the

bulk solution, the concentrated solution moved down from the cotton. This is achieved by introducing a significant number of –OH groups at the molecular level into the backbone structure of the sp^{2}C-CPPs, rendering it highly hydrophilic. Additionally, the large pore structure of the aerogel substrate itself facilitates the construction of numerous water channels that promote efficient salt circulation because the water channels can enhance the diffusion and convection of salt ions under the action of concentration gradients (Fig. 3B and C). Then, the practical applications of sp^{2}C-CPPs for solar-light-driven desalination and water treatment were further explored. The seawater quality of the treated water was assessed using inductively coupled plasma mass spectrometry (ICP-MS). Following desalination through our solar water evaporation system, the concentrations of ions (Na$^+$, K$^+$, Mg^{2+}, and Ca^{2+}) were significantly reduced by three to four orders of magnitude, falling well below the drinking water standards set by the World Health Organization (WHO) (Fig. 3D). Besides seawater, sp^{2}C-CPP based solar evaporation systems can also be used to purify wastewater containing heavy metals. After purification, the concentration of heavy metal ions such as Cr^{3+}, Cu^{2+}, Ni^{2+}, Zn^{2+}, and Ga^{3+} was reduced to $\sim$0.1 ppm (Fig. 3E). By comparison, it also can be seen that the evaporation rate of the sp^{2}C-CPP aerogel evaporator in this work is higher than the average level of two-dimensional materials (1.42 kg m^{-2} h^{-1}) (Fig. 3F and Table S1, refer to the ESI†).

The synergistic effect of photothermal and photocatalysis for uranium extraction

Photocatalytic technology as an environmentally friendly, and efficient method has been extensively used for uranium
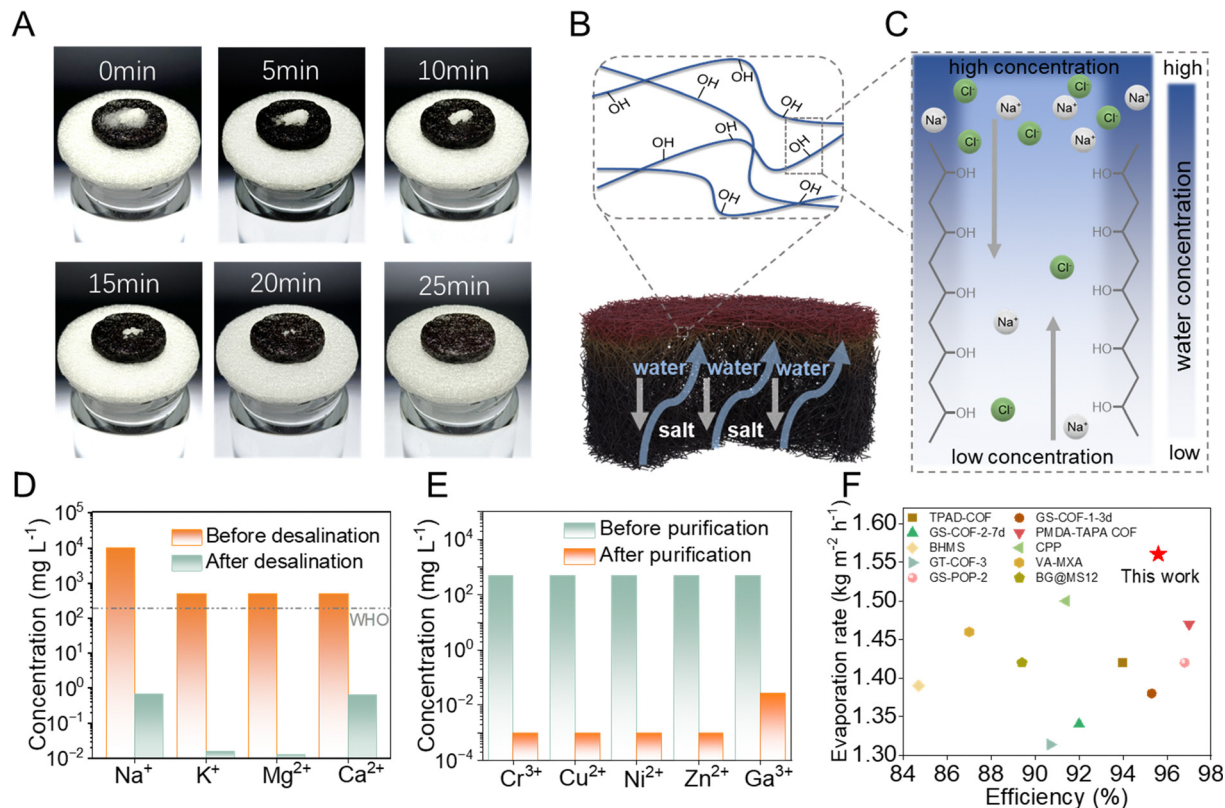
Fig. 3 (A) Digital photographs of a salt self-excreting salt progression of DHA-TMT CPP aerogels under ambient conditions. (B) and (C) Schematic diagram showing the salt transport in seawater below the evaporator. (D) Ion concentration of simulated seawater before and after desalination. (E) Heavy ion concentration before and after purification. (F) Comparison of evaporation performance and photothermal conversion efficiency of different evaporators based on two-dimensional materials previously reported.

recovery from natural seawater and solar-driven photothermal effects are considered to have significant potential in enhancing the coordination between uranium and binding sites[48] (Fig. 4A). UV-vis absorption spectroscopy and Mott–Schottky plots were conducted to assess the optical properties of the two sp^2C-CPP aerogels (Fig. 4B and Fig. S15, ESI†). The band gaps of the two sp^2C-CPPs were 1.34 eV (DHA-TMT) and 1.49 eV (DBD-TMT), respectively, obtained by their corresponding Tauc plots (Fig. S10, ESI†). Combining with conduction band (E_{CB}) values (−0.898 eV and −0.93 eV) determined *via* the x-intercept of the Mott–Schottky plots, we obtain the conduction band (E_{VB}) values of 0.442 eV and 0.56 eV, based on the equation: $E_{VB} = E_{CB} + E_g$. Since these values are more positive than that of U(VI), the photogenerated electrons of both sp^2C-CPPs are thermodynamically permitted to generate a reduction of soluble U(VI) to insoluble U(IV) (Fig. 4C). Encouraged by the above results, further investigations were conducted to explore the photocatalytic uranium capture performance of the two sp^2C-CPP aerogels. All the experiments were conducted under simulated seawater conditions (pH = 8.2) to account for the simultaneous occurrence of photothermal desalination and uranium extraction from seawater. Firstly, we tested the uranium capacity of SiO_2 aerogel substrate in the same condition. The results indicate that uranium capture by SiO_2 substrate almost negligible (Fig. S17, ESI†). Significantly, under simulated sunlight irradiation, the uranium capture capacities of both sp^2C-CPP aerogels sharply

increased from 280 mg m⁻² and 240 mg m⁻² to 1200 mg m⁻² (DHA-TMT) and 880 mg m⁻² (DBD-TMT), respectively (Fig. 4D). And the extraction performance of uranium from DHA-TMT aerogel is significantly superior than DBD-TMT aerogel, which is consistent with the results of photothermal experiments mentioned above. This can be attributed to the highly conjugated hydroquinone group present in the donor unit, which significantly narrows the band gap and enhances charge transfer efficiency, resulting in higher photocatalytic uranium extraction capacity. Moreover, the photothermal effect elevates the overall temperature and accelerates the movement of uranyl ions, which further accelerates the extraction efficiency of uranium. Furthermore, the kinetic investigations indicate that the Langmuir model better fits the equilibrium adsorption isotherm, proving that photocatalytic uranium extraction is a chemical adsorption process (Fig. 4E and Fig. S18 and 19, ESI†). We performed calculations to determine the electron distribution in the highest occupied molecular orbitals (HOMOs) and lowest unoccupied molecular orbitals (LUMOs) of the sp^2C-CPPs. The results indicate efficient electron injection from the π-conjugated backbone into the electrophilic triazine unit, facilitating enhanced separation of photogenerated electrons (Fig. 4F).

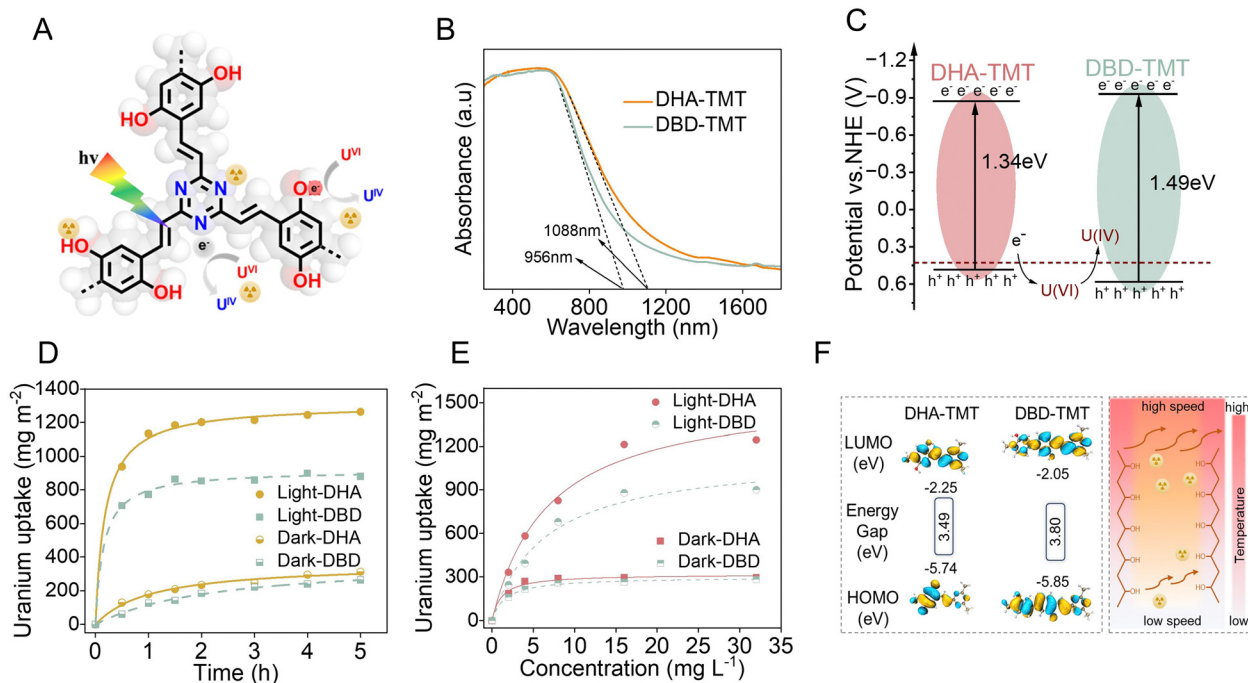Furthermore, DHA-TMT exhibits a narrower band gap in its HOMO–LUMO energy levels compared to DBD-TMT, suggesting

Fig. 4 (A) Schematic diagram of the proposed mechanism for DHA-TMT to capture uranium. (B) UV-vis absorption spectra of DHA-TMT and DBD-TMT. (C) Band structure diagram of DHA-TMT and DBD-TMT aerogels. (D) Adsorption kinetics of uranium on DHA-TMT and DBD-TMT aerogels. Experimental conditions: pH = 8.2, initial U(vi) = 16 ppm. (E) Adsorption isotherm of uranium on DHA-TMT and DBD-TMT. Experimental conditions: pH = 8.2. (F) The excited state electronic structures of DHA-TMT and DBD-TMT aerogels and schematic of the effect of temperature on the rate of motion of uranium ions.

superior electron mobility. Moreover, the emergence of new intense U 4f double peaks in the complete XPS spectra of both sp^{2}C-CPP adsorbents, under both sunlight irradiation and dark conditions, provides compelling evidence for the formation of UO$_2$ (Fig. S20a and b, ESI†). Also, the U 4f peaks were more pronounced after uranium adsorption in the light than in the dark. Meanwhile, the peaks for U $4f^{7/2}$ (382.01 and 381.87 eV) and U $4f^{5/2}$ (392.8 and 392.8 eV) in the high-resolution U 4f XPS spectra of DHA-TMT-U and DBD-TMT-U demonstrated that U(vi) and U(iv) coexisted after uranium binding both in the dark and under visible light irradiation, proving that U(vi) was reduced to U(iv) during the sorption of DHA-TMT and DBD-TMT (Fig. S20c and d, ESI†). Finally, following five cycles, the regenerated aerogel demonstrated a uranium adsorption capacity of 865 mg m^{-2}, representing 75.5% of the initial capacity. This indicates that it can be effectively utilized for uranium adsorption in seawater environments over extended periods (Fig. S21, ESI†)

Conclusions

In summary, we show the synthesis of three-dimensional porous sp^{2}C-CPP-based aerogels through surface-initiated aldol polycondensation. Owning to the extended π-conjugated structure and electron-donating groups (–OH), the as-prepared sp^{2}C-CPP-based aerogels exhibit superior photothermal and photocatalytic performance. Under visible-light irradiation, the DHA-

TMT-based aerogels showed high light-to-thermal conversion efficiency (~95.6%) and water evaporation rate (~1.55 kg m^{-2} h^{-1}) in simulated seawater. The sp^{2}C-CPP aerogels also exhibit an exceptional resistance to salt with no visible salt crystals on the surface of the aerogels even in 25% brine and under 10 cycles. Meanwhile, the DHA-TMT-based aerogels exhibit exceptional photothermal conversion efficiency, which significantly enhances ion transfer. The uranium extraction ability through the fast mass transfer caused by photothermal conversion improves the original adsorption capacity from 280 (under dark) to 1200 mg m^{-2}. This work demonstrated an effective SI-AP approach to constructing robust sp^{2}C-CPP-based aerogels and provided promising three-dimensional porous materials for sunlight-driven seawater desalination and uranium extraction.

Data availability

All data of this study are available within the article and its ESI.†

Conflicts of interest

There are no conflicts to declare.

Acknowledgements

References

1 J. A. Martín-Illán, D. Rodríguez-San-Miguel, O. Castillo, G. Beobide, J. Perez-Carvajal, I. Imaz, D. Maspoch and F. Zamora, *Angew. Chem., Int. Ed.*, 2021, **60**, 13969–13977.

2 W. Zhang, H. Zuo, Z. Cheng, Y. Shi, Z. Guo, N. Meng, A. Thomas and Y. Liao, *Adv. Mater.*, 2022, **34**, 2104952.

3 N. B. McKeown and P. M. Budd, *Chem. Soc. Rev.*, 2006, **35**, 675–683.

4 M. Wang, P. Zhang, X. Liang, J. Zhao, Y. Liu, Y. Cao, H. Wang, Y. Chen, Z. Zhang, F. Pan, Z. Zhang and Z. Jiang, *Nat. Sustain.*, 2022, **5**, 518–526.

5 M. Barawi, L. Collado, M. Gomez-Mendoza, F. E. Oropeza, M. Liras and V. A. de la Peña O'Shea, *Adv. Energy Mater.*, 2021, **11**, 2101530.

6 N. Hüsing and U. Schubert, *Angew. Chem., Int. Ed.*, 1998, **37**, 22–45.

7 F. Rechberger, F. J. Heiligtag, M. J. Süess and M. Niederberger, *Angew. Chem., Int. Ed.*, 2014, **53**, 6823–6826.

8 L. Chen, X. Yu, M. Gao, C. Xu, J. Zhang, X. Zhang, M. Zhu and Y. Cheng, *Chem. Soc. Rev.*, 2024, **53**, 7489–7530.

9 X. Hu and J. Zhu, *Adv. Funct. Mater.*, 2020, **30**, 1907234.

10 C. Li, S. Cao, J. Lutzki, J. Yang, T. Konegger, F. Kleitz and A. Thomas, *J. Am. Chem. Soc.*, 2022, **144**, 3083–3090.

11 A. Jrad, M. A. Olson and A. Trabolsi, *Chem*, 2023, **9**, 1413–1451.

12 Y. Zhao, S. Li, G. Fu, H. Yang, S. Li, D. Wu and T. Zhang, *ACS Cent. Sci.*, 2024, **10**, 775–781.

13 S. Li, Y. Geng, B. Teng, S. Xu, P. S. Petkov, Z. Liao, B. Jost, Y. Liu, X. Feng, B. Wu and T. Zhang, *Chem. Mater.*, 2023, **35**, 1594–1600.

14 H. L. Nguyen, N. Hanikel, S. J. Lyle, C. Zhu, D. M. Proserpio and O. M. Yaghi, *J. Am. Chem. Soc.*, 2020, **142**, 2218–2221.

15 A. Mei, H. Guo, W. Zhang, Y. Liu and W. Chen, *Small*, 2024, 2403521.

16 X. Guo, Y. Li, M. Zhang, K. Cao, Y. Tian, Y. Qi, S. Li, K. Li, X. Yu and L. Ma, *Angew. Chem., Int. Ed.*, 2020, **59**, 22697–22705.

17 N. A. Mazlan, A. Lewis, F. S. Butt, R. Krishnamoorthi, S. Chen and Y. Huang, *Front. Chem. Sci. Eng.*, 2024, **18**, 89.

18 J. A. Martín-Illán, D. Rodríguez-San-Miguel, O. Castillo, G. Beobide, J. Perez-Carvajal, I. Imaz, D. Maspoch and F. Zamora, *Angew. Chem., Int. Ed.*, 2021, **60**, 13969–13977.

19 S.-C. Li, B.-C. Hu, Y.-W. Ding, H.-W. Liang, C. Li, Z.-Y. Yu, Z.-Y. Wu, W.-S. Chen and S.-H. Yu, *Angew. Chem., Int. Ed.*, 2018, **57**, 7085–7090.

20 B.-C. Hu, H.-R. Zhang, S.-C. Li, W.-S. Chen, Z.-Y. Wu, H.-W. Liang, H.-P. Yu and S.-H. Yu, *Adv. Funct. Mater.*, 2023, **33**, 2207532.

21 C. Ziegler, A. Wolf, W. Liu, A.-K. Herrmann, N. Gaponik and A. Eychmüller, *Angew. Chem., Int. Ed.*, 2017, **56**, 13200–13221.

22 X. Li, Z. Jia, J. Zhang, Y. Zou, B. Jiang, Y. Zhang, K. Shu, N. Liu, Y. Li and L. Ma, *Chem. Mater.*, 2022, **34**, 11062–11071.

23 D. Zhu, Y. Zhu, Q. Yan, M. Barnes, F. Liu, P. Yu, C.-P. Tseng, N. Tjahjono, P.-C. Huang, M. M. Rahman, E. Egap, P. M. Ajayan and R. Verduzco, *Chem. Mater.*, 2021, **33**, 4216–4224.

24 H. Fan, J. Gu, H. Meng, A. Knebel and J. Caro, *Angew. Chem., Int. Ed.*, 2018, **57**, 4083–4087.

25 K. Wang, H. Yang, Z. Liao, S. Li, M. Hambsch, G. Fu, S. C. B. Mannsfeld, Q. Sun and T. Zhang, *J. Am. Chem. Soc.*, 2023, **145**, 5203–5210.

26 Y. Chen, S. Li, X. Pei, J. Zhou, X. Feng, S. Zhang, Y. Cheng, H. Li, R. Han and B. Wang, *Angew. Chem., Int. Ed.*, 2016, **55**, 3419–3423.

27 W.-R. Cui, C.-R. Zhang, R.-P. Liang and J.-D. Qiu, *J. Mater. Chem. A*, 2021, **9**, 25611–25620.

28 W.-R. Cui, C.-R. Zhang, R.-P. Liang, J. Liu and J.-D. Qiu, *ACS Appl. Mater. Interfaces*, 2021, **13**, 31561–31568.

29 Y. Zhang, S. Yuan, X. Feng, H. Li, J. Zhou and B. Wang, *J. Am. Chem. Soc.*, 2016, **138**, 5785–5788.

30 S. Zhao, G. Siqueira, S. Drdova, D. Norris, C. Ubert, A. Bonnin, S. Galmarini, M. Ganobjak, Z. Pan, S. Brunner, G. Nyström, J. Wang, M. M. Koebel and W. J. Malfait, *Nature*, 2020, **584**, 387–392.

31 J. Wang, D. Yuan, P. Hu, Y. Wang, J. Wang and Q. Li, *Adv. Funct. Mater.*, 2023, **33**, 2300441.

32 A. Acharjya, P. Pachfule, J. Roeser, F.-J. Schmitt and A. Thomas, *Angew. Chem., Int. Ed.*, 2019, **58**, 14865–14870.

33 Y. Yamashita, T. Yasukawa, W.-J. Yoo, T. Kitanosono and S. Kobayashi, *Chem. Soc. Rev.*, 2018, **47**, 4388–4480.

34 C.-P. Niu, C.-R. Zhang, X. Liu, R.-P. Liang and J.-D. Qiu, *Nat. Commun.*, 2023, **14**, 4420.

35 S. Li, R. Ma, S. Xu, T. Zheng, G. Fu, Y. Wu, Z. Liao, Y. Kuang, Y. Hou, D. Wang, P. S. Petkov, K. Simeonova, X. Feng, L.-Z. Wu, X.-B. Li and T. Zhang, *J. Am. Chem. Soc.*, 2022, **144**, 13953–13960.

36 G. Fu, D. Yang, S. Xu, S. Li, Y. Zhao, H. Yang, D. Wu, P. S. Petkov, Z.-A. Lan, X. Wang and T. Zhang, *J. Am. Chem. Soc.*, 2024, **146**, 1318–1325.

37 W.-R. Cui, F.-F. Li, R.-H. Xu, C.-R. Zhang, X.-R. Chen, R.-H. Yan, R.-P. Liang and J.-D. Qiu, *Angew. Chem., Int. Ed.*, 2020, **132**, 17837–17843.

38 J. Xu, C. Yang, S. Bi, W. Wang, Y. He, D. Wu, Q. Liang, X. Wang and F. Zhang, *Angew. Chem., Int. Ed.*, 2020, **59**, 23845–23853.

39 T. Li, J. Xiong, M. Chen, Q. Shi, X. Li, Y. Jiang, Y. Feng and B. Zhang, *Front. Chem. Sci. Eng.*, 2024, **18**, 3.

40 Y. Zhang, W. Lv, F. Wang, X. Niu, G. Wang, X. Wu, X. Zhang and X. Chen, *Front. Chem. Sci. Eng.*, 2023, **17**, 548–556.

41 S. Li, R. Ma, S. Xu, T. Zheng, H. Wang, G. Fu, H. Yang, Y. Hou, Z. Liao, B. Wu, X. Feng, L.-Z. Wu, X.-B. Li and T. Zhang, *ACS Catal.*, 2023, **13**, 1089–1096.

42 W.-R. Cui, C.-R. Zhang, R.-H. Xu, X.-R. Chen, W. Jiang, Y.-J. Li, R.-P. Liang, L. Zhang and J.-D. Qiu, *Appl. Catal., B*, 2021, **294**, 120250.

43 G. Fu, H. Yang, W. Zhao, P. Samorì and T. Zhang, *Adv. Mater.*, 2024, 2311541.

44 L. Liang, Y. Zhao, W. Zhang, H. Yan, M. Chen, Y. Chen, J. Zhou and T. Zhang, *Chem. Eng. J.*, 2024, **496**, 153894.

45 E. Jin, Z. Lan, Q. Jiang, K. Geng, G. Li, X. Wang and D. Jiang, *Chem*, 2019, **5**, 1632–1647.

46 C. Li, S. Cao, J. Lutzki, J. Yang, T. Konegger, F. Kleitz and A. Thomas, *J. Am. Chem. Soc.*, 2022, **144**, 3083–3090.

47 X. Kong, Z. Wu, M. Strømme and C. Xu, *J. Am. Chem. Soc.*, 2024, **146**, 742–751.

48 T. Li, X. Lin, Z. Zhang, L. Yang, Y. Qian, L. Fu, S. Zhou, W. Chen, Q. Wang, X. Li, X.-Y. Kong, H. Xiao, L. Jiang and L. Wen, *Adv. Funct. Mater.*, 2023, **33**, 2212819.